




# Importance of CdS buffer layer thickness on $\text{Cu}_2\text{ZnSnS}_4$ -based solar cell efficiency

A Cantas<sup>1,2</sup>, F Turkoglu<sup>1</sup>, E Meric<sup>1</sup>, F G Akca<sup>1</sup>, M Ozdemir<sup>3</sup>, E Tarhan<sup>1</sup>, L Ozyuzer<sup>1,3</sup> and G Aygun<sup>1</sup>

<sup>1</sup> Department of Physics, Izmir Institute of Technology, Urla 35430, Izmir, Turkey

<sup>2</sup> Department of Electric and Energy, Pamukkale University, Kınıklı 20160, Denizli, Turkey

<sup>3</sup> Teknoma Technological Materials Inc., Izmir Technology Development Zone, Urla 35430, Izmir, Turkey

E-mail: [as.cantas@gmail.com](mailto:as.cantas@gmail.com) and [aytencantas@iyte.edu.tr](mailto:aytencantas@iyte.edu.tr)

Received 15 February 2018, revised 13 May 2018

Accepted for publication 30 May 2018

Published 19 June 2018



CrossMark

## Abstract

$\text{Cu}_2\text{ZnSnS}_4$  (CZTS) thin films were grown on Mo-coated soda lime glass (SLG) substrates by the sulfurization of DC magnetron-sputtered Zn, Sn and Cu metallic precursors under a sulfur atmosphere at 550 °C for 45 min. Understanding the composition and structure of the CZTS absorber layer is necessary to obtain efficient solar cells. With this aim, x-ray diffractometry, Raman spectroscopy, scanning electron microscopy, energy dispersive spectroscopy and x-ray photoelectron spectroscopy were used to investigate the CZTS absorber layers. CZTS absorber films were obtained and found to be Cu-poor and Zn-rich in composition, which are both qualities desired for efficient solar cells. CdS was used as a buffer layer and was grown by the chemical bath deposition technique. The optical properties of CdS films on SLG were searched for using a spectroscopic ellipsometer and the results revealed that the bandgap increases with film thickness increment. CZTS-based solar cells with different CdS buffer layer thicknesses were prepared using a SLG/Mo/CZTS/CdS/ZnO/AZO solar cell configuration. The influence of the CdS buffer layer thickness on the performance of the CZTS solar cells was investigated. Device analysis showed that electrical characteristics of solar cells strongly depend on the buffer layer's thickness. Highly pronounced changes in  $V_{OC}$ , fill factor and  $J_{SC}$  parameters, which are the main efficiency limiting factors, with changing buffer layer thicknesses were observed. Our experiments confirmed that decreasing the CdS thickness improved the efficiency of CZTS solar cells down to the lowest thickness limit.

Keywords: CZTS, thin film solar cells, CBD, CdS, magnetron sputtering, XPS

(Some figures may appear in colour only in the online journal)

## 1. Introduction

Most of the current photovoltaic (PV) industry is based on crystalline silicon (c-Si) solar cells [1]. Although silicon technology has the highest industrial photoconversion efficiency of 26.3% [2], the indirect bandgap of Si causes low absorption rates, thus limiting the performance of these solar cells. Therefore, light absorbing Si layers should have a thickness of more than 150 nm for highly efficient solar cells. Furthermore, their crystal structure should be nearly monocrystalline which increases their production cost. On the other hand, interest in thin film solar cells is rapidly growing since they provide

a cost effective alternative to Si-based cells. Thin film solar cells have direct bandgaps and are 100 times thinner than c-Si solar cells, which decreases their production cost. Among the thin film solar cells, the highest efficiency of 22.6% has been recorded for chalcopyrite  $\text{Cu}(\text{In,Ga})\text{Se}_2$  (CIGSe) absorber layers [3] which is comparable to c-Si solar cells. CdTe follows CIGS with 22.1% photoconversion efficiency [4, 5]. Although commercially available CIGS and CdTe solar cells are considered to be the two major thin film solar cell technologies, there are some concerns about constituent elements of these absorbers. The rareness of Ga, Te and In in the Earth's crust as well as the toxicity of Se and Cd limit

the mass production and widespread use of CIGS and CdTe solar cells. Therefore, in the last few years, research into abundantly available and non-toxic solar cells has been increased to overcome these limitations. For the second-generation PV materials, the quaternary kesterite type semiconductor compounds have been considered as a promising candidate due to their similar structural and optical properties to those of CIGS thin films. In particular,  $\text{Cu}_2\text{ZnSn}(\text{SSe})_4$  (CZTSSe) thin films, which are the main focus of this research, are p-type semiconductor compounds with a kesterite structure. The elemental constituents of CZTSSe are not only non-toxic, but also earth-abundant in nature, hence inexpensive. Moreover, CZTSSe thin films have high optical absorption coefficients ( $>10^4 \text{ cm}^{-1}$ ) and direct optical bandgap energies from 1.0 to 1.5 eV (from pure selenium to pure sulfur compounds) [6] which are favorable values for PV applications. To date, the highest recorded power conversion efficiencies of kesterite solar cells in the lab-scale are 12.7% [7], 11.6% [8] and 9.4% [9] for CZTSSe, CZTSe and CZTS, respectively. However, they are still much lower than the theoretically predicted Shockley–Queisser limit which suggests that the maximum possible solar conversion efficiency is at about 33.7% ( $J_{\text{SC}} = 29.6 \text{ mA cm}^{-2}$ ,  $V_{\text{OC}} = 1.23 \text{ V}$ , fill factor (FF) = 90%) for a single p-n junction absorber with a bandgap of 1.4 eV for the AM1.5 solar spectrum. Although still far from this theoretical limit, research into higher efficiencies in kesterite thin film solar cells is rapidly increasing [10]. There are several reasons for the poorer photoconversion efficiencies of CZTS-based solar cells than those in their In and Ga incorporated counterpart (CIGS). Firstly, it is difficult to grow high-quality kesterite films since kesterite compounds have low thermal stability at high temperatures ( $>500 \text{ }^\circ\text{C}$ ) [11]. Secondly, they have a single phase only in a very narrow region in their phase diagrams. In our previous report, it was shown that the uniformity and density of the CZTS films increased for sulfurization temperatures between  $550 \text{ }^\circ\text{C}$ – $570 \text{ }^\circ\text{C}$  [12]. High-temperature annealings of CZTS resulted in decomposition. It has been demonstrated that CZTS decomposes into solid  $\text{Cu}_2\text{S}$  and  $\text{ZnS}$  due to the evaporation of  $\text{SnS}$  and  $\text{S}$  from the film. As a result of this decomposition, Sn-depleted surfaces, Sn vacancies, and  $\text{Cu}_2\text{S}$  and  $\text{ZnS}$  secondary phases are formed [13], which are not suitable for the formation of the p-n junction. Therefore, reducing the Sn loss during the annealing process is highly important for the formation of the CZTS structure. Other major challenges involve phase controlling and the fabrication of defect-free materials. Since CZTS films have very narrow phase stability, they can easily form secondary phases and defects during their production. However, applying chemical etching by immersing them in potassium cyanide (KCN) [14] and HCl [15], the binary  $\text{Cu}_2\text{S}$ ,  $\text{ZnS}$  secondary phases and in bromine in a methanol solution, the ternary  $\text{Cu}_2\text{SnS}_3$  [16] secondary phase can easily be removed. Correlating the formation energies and their transition levels, it is possible to identify a variety of defects in CZTS. Most of them are not favorable for producing a p-type CZTS since they form shallow donor levels, mid-gap states, and deep trap levels. It has been reported that copper vacancies ( $V_{\text{Cu}}$ ) improve the p-type character of CZTS absorber films by forming a shallow

acceptor level just above the valence band maximum. Another acceptor level is formed by the copper on a zinc antisite ( $\text{Cu}_{\text{Zn}}$ ) defect. But the formation energy of this defect is higher than  $V_{\text{Cu}}$  [1] and it forms a deep defect level which is not favorable for PV applications [17]. This means that copper vacancies possess the shallowest acceptor level making the p-type behavior of CZTS sensitive to Cu content. It has been shown that the off-stoichiometric CZTS solar cells have exhibited higher efficiencies than the stoichiometric ones, which indicates that  $V_{\text{Cu}}$  has a strong effect on the p-type nature of CZTS. Cu-poor ( $\text{Cu}/\text{Zn} + \text{Sn} \sim 0.8$ ) and Zn-rich ( $\text{Zn}/\text{Sn} \sim 1.2$ ) composition is desired for highly efficient CZTS based solar cells [17]. In CZTS, these shallow acceptor defects can also form electrically neutral self-compensated defect complexes such as  $[\text{Cu}_{\text{Zn}}^- + \text{Zn}_{\text{Cu}}^+]$  and  $[\text{V}_{\text{Cu}}^- + \text{Zn}_{\text{Cu}}^+]$ . The deep levels are passivated by these defect complexes and as a result, the recombination rate is reduced in the PV device.

It has been reported that CZTS only has a p-type characteristic because  $\text{Cu}_{\text{Zn}}$  shallow acceptor defects are highly stable according to defect formation energy calculations [17]. For all the reasons mentioned above and others, CZTS might be an ideal candidate to produce thin film solar cells, which might replace CIGS in a decade's time. Various techniques such as evaporation [18], sputtering [19], pulsed laser deposition [20], chemical vapor deposition [21], spray pyrolysis [22], spin-coating [23], and electrochemical deposition [24] have been reported for the growth of CZTS absorber films. Among these, the sputtering technique is extensively preferred due to the availability of the thickness control of the metallic precursor, the large area growth occurring at one time, and the reproducible fabrication. In the literature, a CZTS solar cell with the highest efficiency ( $\eta = 9.4\%$ ) has been grown by a sputtering technique [9]. In this research as well, the magnetron sputtering technique was used for the first stage of the growth of CZTS films.

Since the electronic performance of semiconductor devices depends highly on their crystal structures, deviations from stoichiometry and the existence of several phases in the material, knowledge of structural and compositional characteristics of CZTS absorber films is very important for understanding their device properties. For that reason, we have studied and presented such characteristics of our CZTS films in detail. The optical properties of the CdS buffer layer is also highly important in terms of absorption within this layer. Thus, the thickness dependence of optical properties of the CdS buffer was investigated by depositing CdS on a soda lime glass (SLG) substrate.

The particular objective of this research is to build a clear understanding of the effect of the CdS buffer layer thickness on the photoconversion efficiency of CZTS-based solar cells.

## 2. Experimental methods

### 2.1. Absorber layer preparation

In this study, Mo-coated SLGs were used as substrates.  $1 \mu\text{m}$  thick Mo back contacts were deposited in bilayers by a DC magnetron-sputtering technique from two-inch-targets of

Mo with a purity of 99.95%. The Mo-coated SLG substrates were cleaned by ultrasonication in acetone, ethanol, and distilled water for 5 min each, and then exposed to N<sub>2</sub> plasma for 15 min at a 100 W RF bias. CZTS absorber layers with thickness between 1.2 and 1.4 μm were grown by a two-step process. In the first step, metallic precursors were deposited sequentially by a multi-target DC magnetron-sputtering system on Mo-coated SLG substrates. Our multi-target DC magnetron-sputtering system consists of two-inch targets of Cu (99.999%), Sn (99.999%), and Zn (99.99%), and 41 W, 40 W, and 20 W DC powers were used for each target in the respected order during a growth. The target-to-substrate distance was fixed at 8 cm. For the deposition of each metal layer, the substrate holder was rotated towards the related target. Before the sputtering, the vacuum chamber was evacuated down to about 10<sup>-6</sup> Torr pressures by a turbo molecular pump. Heating was not applied to the substrates during the sputtering. After reaching the required pressure levels, a constant flow rate of 30 sccm Ar gas was let into the chamber using a mass flow controller during the deposition process. The operating pressure was 1.5 × 10<sup>-2</sup> Torr. Before the actual growth, a pre-sputtering was performed for 5 min to remove contaminations from the surfaces of the targets. Since the thickness of each metallic precursor layer plays an important role in the formation of a particular CZTS compositional structure, the thickness of each metallic layer was determined using the molecular weight and density of each element before the deposition. Therefore, the thickness of each metallic layer was adjusted as 175, 165 and 290 nm for the Cu, Zn and Sn layers, respectively, to obtain a 630 nm thick metallic precursor. These thicknesses were chosen by considering the Cu-poor and Zn-rich composition which has been reported for the highly efficient CZTS-based solar cells in the literature. The stacking order of the precursor was selected as SLG/Mo/Cu (120 nm)/Sn/Zn/Cu (55 nm) in order to decrease the Sn loss and to prevent ZnS phase formation at the surface of the absorber layer during the sulfurization.

The second step was followed by a heat treatment of metallic precursors under a sulfur atmosphere. This step is called the sulfurization process and it is used to convert metallic stacks of CZT to the CZTS absorber film. The sulfurization procedure was performed in a Lindberg/Blue M furnace under an Ar atmosphere (figure 1(a)). The Cu–Zn–Sn (CZT) precursor was placed at the center of a quartz tube in the furnace while the 600 mg sulfur powder (99.98%) was placed 18 cm away from the precursor in the quartz tube. Sulfurization occurred as a result of the reaction between the evaporated sulfur and the hot metallic precursor. 100 sccm Ar, which was controlled using a MKS 647C mass flow controller, was used as a carrier gas while the pressure inside the quartz tube was kept at atmospheric pressure during the sulfurization.

Figure 1(b) shows the temperature variation of the sulfurization process. The furnace was heated to 270 °C in five min at a constant rate and kept at this temperature for three min to ensure the formation of binary phases such as CuS, ZnS and SnS<sub>2</sub> which contribute to the formation of the CZTS structure. Then, the temperature of the furnace was raised to 550 °C within five min. A thermocouple was located at the center of the

tubular furnace, so it was possible to measure the temperature in the middle of furnace. When the middle of the furnace was 550 °C, the point (18 cm away from the middle of the furnace) where the sulfur powder was placed was at a lower temperature. Using both a high amount of sulfur powder (600 mg) and placing the sulfur box at the edge of the furnace (the sulfur box was located within the furnace but very close to the outlet of the furnace), the sulfurization took place for 45 min. At the end of the sulfurization, when the furnace was opened it was seen that the melted sulfur still existed. Therefore, the sulfurization of CZTS metallic precursors occurred at 550 °C for 45 min.

Subsequently, the CZTS films were naturally cooled down. Four different CZTS absorber layers were fabricated under the same deposition and sulfurization conditions. CZTS absorber films were named with sample numbers from 1 to 4. Film analyses were performed after the sulfurization process.

The crystalline structures of the CZTS and CdS films were analyzed by a Philipps X'Pert Pro x-ray diffractometry (XRD) system with a Cu K $\alpha$  radiation source ( $\lambda = 1.5406 \text{ \AA}$ ) with a step size of 0.03° and a step time of 1.1 s. For the microstructural characterization, a high-resolution confocal micro-Raman spectroscopy (S&I, MonoVista, employing a Princeton Instruments, Acton SP2750 0.750 m Imaging Triple Grating Monochromator) was used in the back-scattering geometry with a spectral resolution of about 1 cm<sup>-1</sup> at room temperature. An argon ion laser operating at 488 nm (100 mW) and 514 nm (100 mW) was used as the Raman excitation source while a HeNe laser with 632.8 nm of 20 mW power was also employed at times to probe the vibrational modes of the CZTS films to analyze their compositional structure. The system also includes an Olympus BX51 microscope with a computer controlled XYZ stage under the objective. For all the CZTS films, 50× and 100× objectives, giving spot sizes near 3 μm in diameter were used. The spectral data was collected with a CCD detector at about 0.5 cm<sup>-1</sup> max resolution in the visible. A rough scan was carried out using a 150 gr mm<sup>-1</sup> grating first then a high-resolution measurement followed by a 600 gr mm<sup>-1</sup> grating. Occasionally we performed measurements with a 1800 gr mm<sup>-1</sup> grating to see any fine structure. Since our phonon peaks were very broad, we did not need 1800 gr mm<sup>-1</sup> grating scans since they were time consuming. The Raman spectrometer was calibrated by adjusting the main phonon peak of a standard Si sample to 520 cm<sup>-1</sup> (at room temperature) via an internal offset feature of the system. The top view of the CZTS and CdS films and the cross-sectional images of the device structure were taken by a FEI-QuantaFEG 250 scanning electron microscope (SEM). The atomic ratios of the CZTS and CdS films were determined by energy dispersive spectroscopy (EDS; Oxford X-act) which was attached to the SEM. Surface topography was imaged with 5 kV acceleration voltage at different magnifications under high vacuum with an Everhart Thornley detector (ETD) and three-spot size whereas the cross-section images were taken with 5 kV acceleration voltage, with a backscatter electron detector (BSED) and five spot size under low vacuum.

EDS measurements were taken with 15 kV acceleration voltage having 1000x magnification with a 20 μm scaling under high vacuum (HV). X-ray photoelectron spectroscopy

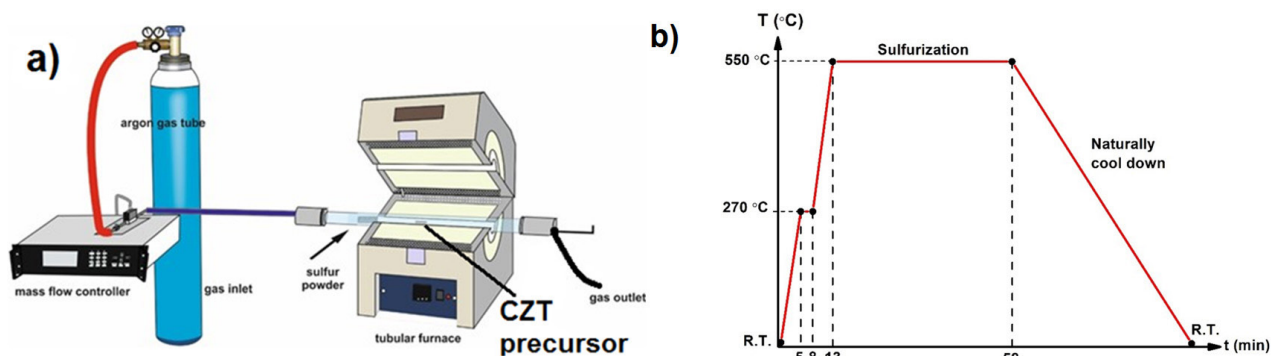


Figure 1. (a) Sulfurization system, (b) temperature variation of sulfurization process.

(XPS; SPECS Phoibos 150 3D-DLD) was used to identify the core electronic states and hence, the quantity of constituent elements. XPS measurements of the CZTS films were performed with a monochromatic Mg  $K\alpha$  radiation source ( $h\nu = 1254\text{ eV}$ ) with a power of 200 W and take off angle of  $45^\circ$ . The analyzer pass energy, the step size, dwell time and the spot size were set to 30 eV, 0.05 eV, 2 s and 2 mm, respectively, for high-resolution spectra.

## 2.2. CdS buffer layer preparation

Prior to fabricating solar cells to analyze the properties of the CdS buffer layer, it was coated on a SLG substrate by the chemical bath deposition (CBD) technique. The bath solution contained 1.2 ml of 0.5 M cadmium acetate ( $\text{Cd}(\text{CH}_3\text{CO}_2)_2$ ), 6 ml of 2M ammonium acetate ( $\text{NH}_4\text{CH}_3\text{CO}_2$ ), 7 ml of 0.5 M thiourea  $\text{SC}(\text{NH}_2)_2$ , and 12 ml of 14.4 M (25% of  $\text{NH}_3$  solution) ammonium hydroxide ( $\text{NH}_4\text{OH}$ ) and 270 ml of de-ionized water. The CdS buffer layers were deposited at  $85^\circ\text{C}$  for 45, 60, 75 and 90 min. The thickness calibration of the CdS films occurred by depositing CdS thin films on SLG substrates by the CBD technique. A spectroscopic ellipsometer (SE) was used to determine the thickness and optical properties of the CdS films deposited on the SLG substrates. Spectroscopic ellipsometry is an optical technique, which is suitable to determine the thickness of semiconductor films [25]. Psi ( $\Psi$ ) and Delta ( $\Delta$ ) are the ellipsometric parameters which measure the phase and amplitude changes of incident light, respectively. In order to define the thickness of the grown film, an appropriate optical model was constructed, and measured and modeled ellipsometric data were fitted [26]. As an optical model for the CdS films, the generalized oscillator (gen-osc) function, which is suitable for semiconductor film, was used. CdS films were modeled using five oscillators. The surface roughness was modeled as a Bruggeman effective approximation (BEMA) layer. With this layer, it was assumed that the top layer of the film consists of a 50% void and 50% CdS film. The thickness and optical constants i.e. refractive index  $n$ , and extinction coefficient  $k$ , were extracted as outcomes of the fitting procedure.

## 2.3. Solar cell device fabrication

For solar cell fabrication, window layers consisting of i-ZnO and Al doped ZnO (AZO) were deposited on SLG/Mo/CZTS/

CdS layer stacks. The window layers of i-ZnO and AZO were deposited using single targets by RF and DC magnetron sputtering, respectively. 40 nm ZnO and 300 nm AZO layers were sputtered with pure argon at around  $10^{-3}$  Torr operation pressure. The solar cells were completed by contacting with silver epoxy on the AZO window layer. The active area of the cells was determined by scribing the regions. According to the CZTS absorber layer used and the CdS buffer layer thickness, the devices were denoted by cell numbers from 1 to 4 (from thickest to thinnest CdS layer). The device performance of the SLG/Mo/CZTS/CdS/ZnO/AZO solar cells was investigated using the current–voltage ( $I$ – $V$ ) measurement system. A Keithley 2182A Source Meter and Labview program were used to obtain  $I$ – $V$  characteristics at room temperature. The calibration of our system was done using a Newport 91192 model 300 W solar simulator under ambient conditions ( $1\text{ kW m}^{-2}$ , AM 1.5G illumination, room temperature).

## 3. Results and discussions

### 3.1. CZTS absorber layer characterizations

**3.1.1. XRD.** CZTS has two types of crystal structure which are named as kesterite (I-4 space group) and stannite (I-42m space group). Since it is a quaternary compound and forms from a solid-state reaction between  $\text{Cu}_2\text{SnS}_3$  and ZnS, it is possible to detect secondary and ternary remaining phases at the end of the growth process. These phases might be ZnS,  $\text{Cu}_{2-x}\text{S}$ ,  $\text{Cu}_2\text{SnS}_3$ , SnS,  $\text{SnS}_2$ , and  $\text{Sn}_2\text{S}_3$ . Except for ZnS and  $\text{Cu}_2\text{SnS}_3$ , all of these phases can be determined by XRD.

However, due to ZnS,  $\text{Cu}_2\text{SnS}_3$ , and CZTS having similar crystal structures, it is very difficult to confirm their existence or co-existence in a sample, merely by the XRD technique [27]. Figure 2 shows the XRD patterns of some of the CZTS films we produced as described above. Since all three CZTS films we show in figure 2 have the same growth parameters, as expected, their XRD patterns are also the same which reflects the reproducibility of the CZTS films. We can generalize this statement to all other CZTS films we produced in the same way whose XRD data are not shown here. All films show some peaks of kesterite CZTS (JCPDS 26-0575) namely,  $\text{Cu}_2\text{SnS}_3$  (JCPDS 027-0198) and/or ZnS (JCPDS 05-0566) at  $28.50^\circ$ ,  $32.99^\circ$ ,  $47.33^\circ$ ,  $56.17^\circ$  and  $58.97^\circ$ . However, all films show characteristic peaks of CZTS along

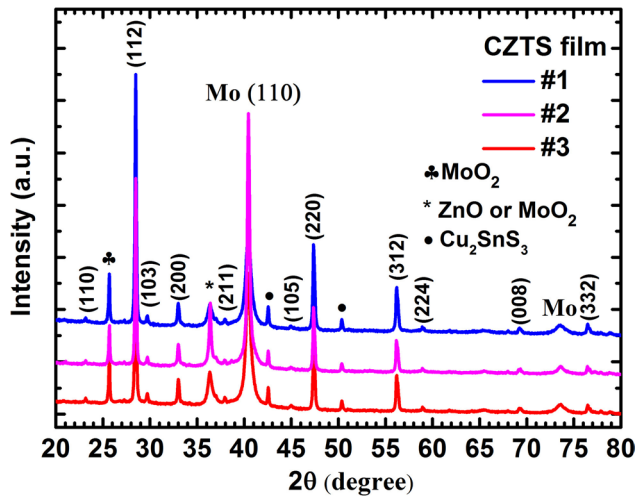


Figure 2. XRD patterns of CZTS sample numbers 1, 2 and 3.

(202), (103), (211), (105), (224), (008) and (332) crystallographic directions at  $37.0^\circ$ ,  $29.67^\circ$ ,  $37.96^\circ$ ,  $44.99^\circ$ ,  $58.97^\circ$ ,  $69.23^\circ$  and  $76.44^\circ$ , respectively (JCPDS 026-0575) which shows that the examined films contain kesterite CZTS structures. In addition to kesterite CZTS, the existence of ZnS and/or  $\text{Cu}_2\text{SnS}_3$  cannot be ruled out. From the patterns of figure 2, the  $\text{Cu}_2\text{SnS}_3$  (CTS) diffraction peaks can be found at  $2\theta$  values of  $42.5^\circ$  and  $50.9^\circ$ , corresponding to the  $(\bar{2}\bar{2}8)$  and  $(\bar{3}\bar{1}9)$  orientations, respectively (JCPDS 027-0198). It is possible to observe a CZTS with a mixture of ZnS and  $\text{Cu}_2\text{SnS}_3$  [28]. The  $\text{Cu}_2\text{S}$  phase which has a diffraction peak at  $45.8^\circ$  [28], was not detected in any of our samples. The XRD patterns of all films exhibit a diffraction peak at  $40.5^\circ$  which is the strongest peak of Mo (110) (JCPDS 042-1120) coming from the back contact. But this peak position also corresponds to  $\text{MoS}_2$  at  $40.99^\circ$ , which has its strongest peak at  $14.4^\circ$  (JCPDS 024-0515) but this value is outside the measurement region of our XRD spectrometer. The diffraction peak at around  $73.60^\circ$  might correspond to the (205) diffraction peak of  $\text{MoS}_2$  at  $73.66^\circ$  (JCPDS 037-1492) and the (211) diffraction peak of Mo at  $73.68^\circ$  (JCPDS 042-1120).

In the XRD spectra, additional peaks which are not related to CZTS, ZnS and  $\text{Cu}_2\text{SnS}_3$ , or any other related secondary phase were detected for all films. The peak observed at  $26.03^\circ$  is attributed to the strongest diffraction peak of  $\text{MoO}_2$  along the  $(\bar{1}\bar{1}1)$  plane (JCPDS 032-0671). The peak detected at  $36.30^\circ$  might be due to a (200)  $\text{MoO}_2$  peak reported to be at  $36.77^\circ$  (JCPDS 032-0671) or a (101) ZnO peak at  $36.25^\circ$  (JCPDS 036-1451). Prior to the deposition of metallic precursors, the Mo-coated SLG substrates were cleaned to get rid of native oxides.

Since Mo is a transitional metal, it is not possible for it to resist oxidation when it is in its natural state, i.e. it can easily oxidize. Because not all deposition and characterization processes were performed in the same system, Mo might be oxidized before placing the substrate into the magnetron sputtering system. Nevertheless, beneficial effects of the  $\text{MoO}_2$  interlayer on the PV performance of CIGS and CZTSe solar cells have been reported [29]. The formation of the  $\text{MoO}_2$

interlayer increased the open circuit voltage ( $V_{OC}$ ) and FF when it exists at a certain amount. For the CZTS, it has been reported that the increase in the oxygen content at the Mo back contact reduces the Mo–S interaction and decreases the  $\text{MoS}_2$  interlayer formation. Thus, the PV characteristic of CZTS is improved by reducing series resistance ( $R_S$ ). Therefore, a 20–30 nm thick  $\text{MoO}_2$  interlayer may improve the back contact interface by reducing the  $\text{MoS}_2$  formation [29].

It is apparent from the XRD patterns that all the samples have good crystallinity and exhibit preferential orientation along the (112) direction with a strong peak at  $28.5^\circ$  which belongs to the kesterite CZTS. The average crystallite size for the strongest CZTS peak along (112) was calculated using Debye–Scherrer’s formula given as [30]

$$D = \frac{0.9 \lambda}{\beta \cos \theta}. \quad (1)$$

Here,  $D$  is the average crystallite size (diameter), the number 0.9 is the particle shape factor for spherical particles (it depends on the shape of the crystalline particles),  $\lambda$  is the wavelength of the Cu- $K_\alpha$  line ( $\lambda = 0.15406$  nm),  $\beta$  is the full width at half maximum (FWHM) of the selected diffraction peak, and  $\theta$  is the Bragg’s angle. Since the FWHM of the (112) plane is approximately the same for all samples, the calculated crystallite sizes are about 50 nm.

**3.1.2. Surface morphology and composition.** The surface morphology of our CZTS films denoted with numbers 1, 2, 3 and 4 were imaged by a SEM, as shown in figure 3. From figure 3, it is seen that all the films have similar surface structures due to the same growth process.

Even though the CZTS films were quite dense, they showed inhomogeneous grain distribution. From the similarities of the surface images and atomic compositions, we can conclude that our films are reproducible under the same growth parameters.

The elemental composition of the CZTS films has been characterized by EDS measurement. The detected atomic concentrations of each constituent elemental and atomic ratios of Cu/(Zn+Sn), Zn/Sn, and S/metal are given in table 1. Because each element composition changes independently from the others, it is hard to tell if the films are ‘Cu-poor’, ‘Zn-rich’ etc. When the S element reacts with the metallic precursor, the amount entering the reaction is based on the quantity of the metal elements and their valence value such as Cu(I), Sn(IV) and Zn(II). Since they are not independent from each other, the atomic percent ratio of Cu/(Zn+Sn) and Zn/Sn is commonly used to describe the composition of CZTS films. In the literature, the experimental results indicate that Cu-poor ( $\text{Cu}/(\text{Zn}+\text{Sn}) \sim 0.8\text{--}0.9$ ) and Zn-rich ( $\text{Zn}/\text{Sn} \sim 1.1\text{--}1.2$ ) compositions are favorable for highly-efficient CZTS-based thin-film solar cells. Cu-poor and Zn-rich composition is desirable to prevent the formation of a detrimental  $\text{Cu}_2\text{S}$  phase,  $\text{Cu}_{\text{Zn}}$  and  $\text{Cu}_{\text{Sn}}$  defects, and  $(\text{Cu}_{\text{Sn}} + \text{Sn}_{\text{Cu}})$  and  $(2\text{Cu}_{\text{Zn}} + \text{Sn}_{\text{Zn}})$  defect complexes [1]. The electrical property of CZTS films is also associated with  $\text{Zn}_{\text{Sn}}$  and  $\text{Sn}_{\text{Zn}}$  defects. For electrically high quality CZTS absorber films, it is necessary to increase the formation of  $\text{Zn}_{\text{Sn}}$  acceptors and to

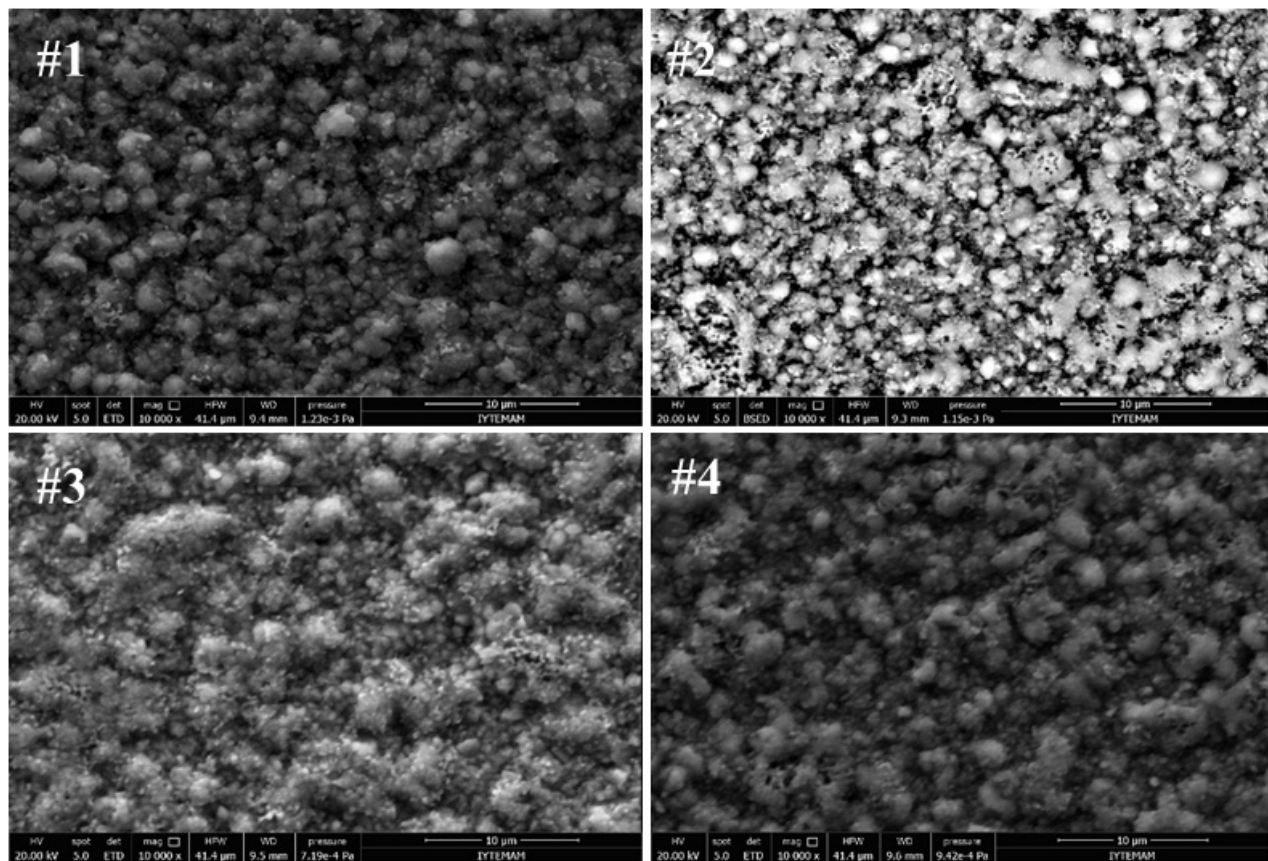


**Figure 3.** SEM surface microstructure of CZTS sample numbers 1, 2, 3 and 4.

**Table 1.** The elemental and compositional ratios (%) of CZTS films determined by EDS.

CZTS film	Atomic (%)				Cu/(Zn+Sn)	Zn/Sn	S/metal
	Cu	Zn	Sn	S			
#1	20.96	13.48	11.09	54.47	0.85	1.22	1.20
#2	20.33	13.41	11.36	54.90	0.82	1.18	1.22
#3	20.72	13.57	11.33	54.37	0.83	1.20	1.19
#4	20.78	13.58	11.20	54.40	0.84	1.21	1.19

diminish the  $\text{Sn}_{\text{Zn}}$  donors. This might be possible when the Zn/Sn ratio is higher than 1 [31].

According to table 1, all CZTS films have generally a Cu-poor and Zn-rich composition despite little deviations from each other.

**3.1.3. Raman spectroscopy.** As mentioned previously, the XRD technique is not adequate alone for the characterization of the structures of CZTS films. Due to the near exact matches in the diffraction spectra of CZTS,  $\text{Cu}_2\text{SnS}_3$ , and ZnS, an additional characterization tool is necessary to identify these phases. Raman spectroscopy is a widely used technique for structural characterization.

It gives vibrational, electronic or rotational internal energy levels of a solid, liquid or gas as the difference between the monochromatic exciting light energy and the scattered light energy. In a typical Raman spectrum, such excitations are displayed as an intensity versus photon energy (difference between incoming and scattered) spectrum. For solid samples

especially, as for our films, the observed Raman peak positions and their intensities of vibrational (phonon) excitations in particular depend strongly on the elemental composition of the solid and are strongly sensitive to the existence of defects in them [32]. In CZTS, the vibrational mode A, which is assigned to the vibrations of sulfur anions in kesterite CZTS, is a characteristic Raman active mode. It generally gives two Raman peaks at 286–287 and 337–338  $\text{cm}^{-1}$ .

Figure 4(a) shows the Raman spectra of all CZTS films 1 to 4 in the spectral region of interest. All of them exhibit very similar broad Raman peaks (bands). The most intense peak lies between 330 and 331  $\text{cm}^{-1}$ . When structural defects exist, peak broadening and a shift of the A mode to a lower frequency side of the Raman spectrum are observed [33]. Although the main A symmetry mode is due to the vibrations of S anions only, the statistical disorder in the nearest Cu and Zn cations is the main cause of the observed widening in the Raman peaks of this mode [34]. This is a commonly encountered case in the literature and the band observed between 330 and 331  $\text{cm}^{-1}$

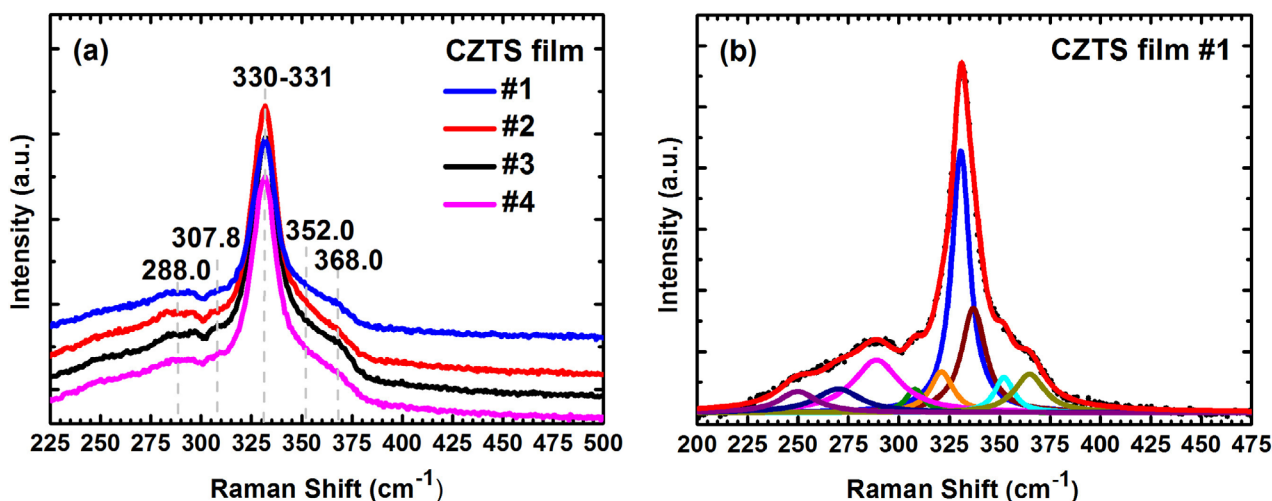


**Figure 4.** (a) Raman spectra of CZTS films 1 to 4, (b) theoretical fit to Raman spectrum of CZTS film 1. The black spheres show the experimental data; Lorentzian curves in different colors represent the synthetic peaks of the spectrum, and the red line gives the envelope of the synthetic peaks.

is assigned to a partially disordered kesterite (PD-KS) phase which is detected in the non-stoichiometric films [35]. The existence of disorder in the Cu and Zn sublattices may change the symmetry of a CZTS crystal from kesterite to disordered kesterite. The peak at nearly  $331\text{ cm}^{-1}$  is observed mostly in the Cu-poor CZTS films with a high concentration of intrinsic structural defects. These defects are Zn antisite defects in the place of Cu atoms ( $\text{Zn}_{\text{Cu}}$ ) and Cu vacancies ( $V_{\text{Cu}}$ ). In addition, the peak seen at  $331\text{ cm}^{-1}$  has been reported to be due to the presence of local structural inhomogeneity within the disordered cation sublattice [36]. By using a neutron diffraction technique, Schorr *et al*, demonstrated the existence of the PD-KS structure by examining the Cu and Zn atoms lying randomly at the Cu+Zn (001) layers [37].

Being neighbors on the periodic table, Cu and Zn atoms have an equal number of electrons and the same atomic form factors, hence x-ray techniques cannot differentiate  $\text{Cu}^+$  and  $\text{Zn}^{2+}$  layers [37].

Raman spectroscopy, on the other hand, is an adequate technique to detect this disorder especially since Raman phonon peaks depend mostly on the atomic masses as well as bond strengths which are different for different type of atoms even in the same lattice environment. In order to obtain a more quantitative analysis, the fitting procedure was only applied to the peaks in the Raman spectrum of CZTS film 1. For the deconvolution process of experimental Raman scattering of CZTS film 1, the Lorentzian line shape function was used. During the fitting, the peak positions were let to change in order to get the best match with the experimental data. Figure 4(b) shows the results of our fitting procedure where the individual Lorentzian peak functions are displayed with different colors and their sum is indicated by the continuous red line. The calculated total peak function (the red line) matches very well with the experimental Raman spectrum (solid black spheres). The deconvolution procedure was quite successful when we assumed that the intense and broad spectral region consisted of two major peaks (one at around  $331\text{ cm}^{-1}$  and the other at around  $337\text{ cm}^{-1}$ ).

**Table 2.** Peak fitting results of main XPS core levels of CZTS film 1.

Sample	Cu $2p_{3/2}$ (eV)	Zn $2p_{3/2}$ (eV)	Sn $3d_{5/2}$ (eV)	1st S $2p_{3/2}$ (eV)	2nd S $2p_{3/2}$ (eV)
CZTS #1	932.0	1021.8	486.4	161.7	162.2

However, crystallization of CZTS in the kesterite structure with some amount of disordered kesterite phase is quite possible. Although the main Raman peak of CZTS should be at about  $337\text{--}338\text{ cm}^{-1}$ , our peak fitting result indicated that the main peak position was at  $330.7\text{ cm}^{-1}$  for film 1. In addition to the PD-KS peak, all films also have two strong peaks at about  $286\text{--}288$  and  $337\text{--}338\text{ cm}^{-1}$  which are assigned to the main vibrational A symmetry modes of KS CZTS. The presence of these peaks indicate that the CZTS films in this work are a mixture of two CZTS phases: namely, PD-KS and KS, which is not very unusual for non-stoichiometric compositions. Since the E and B modes include both anion and cation vibrations, they show longitudinal and transverse optical mode (LO-TO) splittings. The CZTS film 1 also exhibits a peak at  $250\text{ cm}^{-1}$  which is attributed to the B mode of longitudinal optical vibration (B(LO)) vibration of KS CZTS [38]. The peak which was observed directly at  $270\text{ cm}^{-1}$  and better resolved as a result of the deconvolution was attributed to the A vibration mode of KS CZTS [39]. The CZTS film 1 has its major Raman peak at  $307.8\text{ cm}^{-1}$ . The theoretical calculations of Guc *et al* and Khare *et al* reported this mode as the B(TO) vibration of KS CZTS with a peak at  $307.6\text{ cm}^{-1}$  [33, 39]. The shift between the calculated and the experimental peak positions might be based on the LO-TO splitting [39].

A peak at  $320\text{ cm}^{-1}$ , which was not well resolved in the Raman spectrum of CZTS film 1 but which was identified from our peak fitting results has been observed experimentally elsewhere and was assigned to the B(LO) vibration mode of KS CZTS in [33].

The peak detected at  $352\text{ cm}^{-1}$  might be attributed to the ZnS secondary phase or to the B mode of transverse optical vibration (B(TO)) mode of KS CZTS [33] or to the tetragonal

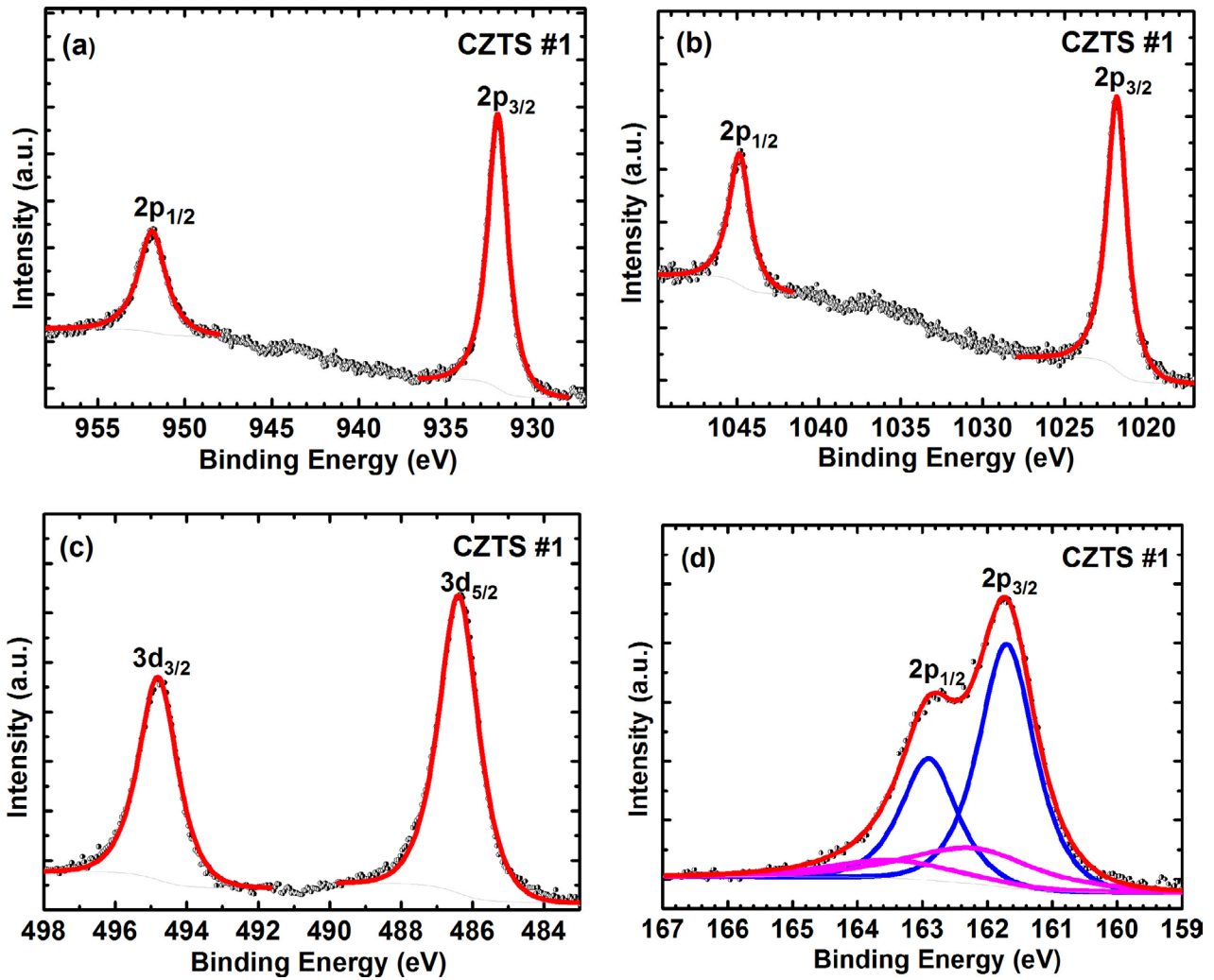


**Figure 5.** High-resolution XPS peak fitting results of CZTS film 1 (a) Cu 2p, (b) Zn 2p, (c) Sn 3d and (d) S 2p valence regions.

$\text{Cu}_2\text{SnS}_3$  (CTS) [40]. Although the main vibration modes of CZTS exhibited intense Raman peaks, the presence of a ZnS secondary phase cannot be ruled out. The formation of a ZnS secondary phase is quite possible in the CZTS films with Zn-rich and Cu-poor composition. In addition, our fitted spectrum gave another contribution at about  $368\text{ cm}^{-1}$  for all samples which was associated with the E(LO) mode of KS CZTS [41]. From the peak observed at  $475\text{ cm}^{-1}$  in the Raman spectra of all CZTS films, the formation of a  $\text{Cu}_2\text{S}$  phase was also evident which supports the XRD analyses spectra. Based on the results of the Raman analysis, we can conclude that the producing CZTS films in a non-stoichiometric composition will cause disorder in the lattice.

**3.14. XPS analysis.** CZTS film 1 was further analyzed with XPS at high resolutions to identify the surface composition and chemical bonding states of the constituent elements.

High-resolution spectra of C 1s, S 2p, Cu 2p, Sn 3d and Zn 2p valence regions were measured in detail and calibrated with respect to the C 1s peak at  $284.6\text{ eV}$  [19]. In order to identify the atomic multivalency of each element in CZTS, the high-resolution spectra were de-convoluted. In addition, the calculation of atomic concentrations of the constituent elements were carried out by the CASAXPS software for which

**Table 3.** The surface quantification of CZTS film 1 by XPS.

Sample	Atomic (%)				Cu/ (Zn + Sn)	Zn/ Sn	S/ metal
	Cu	Zn	Sn	S			
CZTS #1	25.8	19.2	14.9	40.1	0.8	1.3	0.7

the area of peaks and sensitivity factors for each element were used as parameter variables.

Before the de-convolution, a Shirley-type background was subtracted from the high-resolution spectrum of each element and a Gaussian–Lorentzian product GL(p) function was used in accordance with the theoretical assumptions. Due to spin–orbit coupling, the Zn, Cu, S 2p and Sn 3d peaks form as doublets of  $2p_{3/2}$ ,  $2p_{1/2}$  and  $3d_{5/2}$ ,  $3d_{3/2}$ . The 2p spectra was fitted using an  $I(2p_{3/2}):I(2p_{1/2})$  intensity ratio of 2:1 whereas 3d spectra was fitted using an  $I(3d_{5/2}):I(3d_{3/2})$  intensity ratio of 3:2 [19]. During the fitting process, spin–orbit splitting values and the FWHM value of each coupling elements were constrained. However, no constraint on the peak positions was applied. The peak fitting results are listed in table 2. In figure 5(a), the Cu 2p core level is seen as Cu  $2p_{1/2}$  and  $2p_{3/2}$  coupled doublets with a peak splitting of  $19.8\text{ eV}$ , which is indicative of a monovalent copper, Cu (I), which is consistent with the literature [42–44]. As a



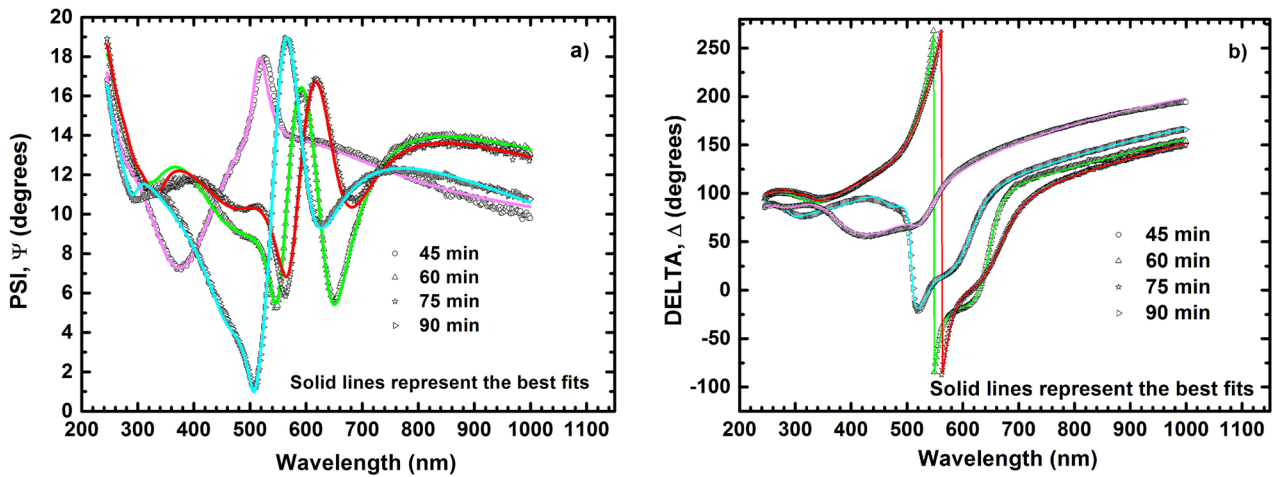


**Figure 6.** Constructed optical model and fitting results of ellipsometric data of CdS films for (a) PSI ( $\Psi$ ), (b) DELTA ( $\Delta$ ). The dashed lines represent the measured data whereas the solid lines represent the fitted result.

technical note, we have used a GL(90) line shape for the Cu  $2p$  spectral region. The Cu  $2p_{3/2}$  peak position was observed at 932.0 eV [45] which confirms that the copper is in the +1 oxidation state Cu(I). The well-known shake up satellite shoulder between 940–945 eV [46], which is a clue about the presence of CuO, was not detected, therefore, the Cu<sup>2+</sup> (Cu(II)) charge state is absent. In the Cu  $2p_{3/2}$  peak spectral region, no peak was detected between 935.0 and 935.5 eV indicating the presence of any CuSO<sub>4</sub> formation [47]. From this, it can be concluded that neither copper oxide nor copper sulfate phases were formed on the film surface.

Figure 5(b) shows the peak fittings in the spectral region of the Zn  $2p$  valence electrons of CZTS film 1. The Zn  $2p$  spectrum was fitted using a GL(90) line shape as well and consists of  $2p_{1/2}$  and  $2p_{3/2}$  peaks with a double separation of 23.0 eV which can be attributed to the bivalent zinc Zn (II) [48]. The  $2p_{3/2}$  peak appeared at 1021.8 eV for the CZTS film 1. This peak could be attributed to the existence of Zn<sup>2+</sup> [46]. The peak position of Zn  $2p_{3/2}$  might be due to Zn in CZTS or Zn in ZnO.

The peak fitting analysis of the Sn  $3d$  core level observed in the spectrum of CZTS film 1 (figure 5(c)) was done according to a GL(55) line shape. The spectrum showed a  $3d_{3/2}$  and  $3d_{5/2}$  doublet with a peak separation of 8.4 eV. As a result of the de-convolution, the Sn  $3d_{5/2}$  peak was identified at 486.4 eV which confirmed the existence of a Sn(IV) charge state as expected in a CZTS formation [49].

In figure 5(d), the spectrum observed in the range of 160 to 164 eV was identified as the  $2p$  spectrum of S in metal sulfides [50]. This spectrum was resolved into two doublets, corresponding to two different phases. During the fitting process a GL(75) line shape was used and each S  $2p_{3/2}$  and  $2p_{1/2}$  doublet was constrained to have a binding energy difference of 1.2 eV. The first detected S  $2p_{3/2}$  peak at 161.7 eV was attributed to a monosulfide S<sup>-2</sup> existence [46, 50], as expected from a CZTS structure. In the  $2p$  spectrum of S in the CZTS film 1, the second  $2p_{3/2}$  peak of S was detected at 162.2 eV which represents a disulfide (S<sub>2</sub><sup>-2</sup>) phase [19] on the surface of the film. After the deconvolution process, the

**Table 4.** Spectroscopic ellipsometric fitting results of CdS thin films.

Deposition time (min)	Sample thickness (nm)	Roughness (nm)
45	85.0	10.0
60	120.0	10.2
75	133.0	10.4
90	148.0	12.1

surface quantification of CZTS film 1 was calculated by the following equation:

$$C_x = \frac{(I_x/S_x)}{\sum I_i/S_i} * 100. \quad (2)$$

Here,  $C_x$ ,  $I_x$  and  $S_x$  are the atomic percentage, the peak area and the atomic sensitivity factor of an element  $x$  which constitutes the sample.  $I_i$  and  $S_i$  are the peak area and the atomic sensitivity factor of the  $i$ th element inside the sample. The quantification of the CZTS surface structure of film 1 is listed in table 3.

From the XPS and EDS results, we conclude that the surface composition of the film has a little deviation from its bulk form.

XPS characterization confirms that the surface of a CZTS film is comprised of Cu, Zn, Sn and S elements. It is also interesting to note that the surface of the film tends to be richer in Sn, Zn, and Cu than the bulk. The reason for the higher Zn concentration at the surface than those the bulk of the CZTS film might be due to the presence of a ZnO phase at the film surface.

### 3.2. CdS buffer layer characterizations

**3.2.1. SE.** In this study, to determine the thickness ( $d$ ), refractive index ( $n$ ) and extinction coefficient ( $k$ ) of the CdS thin films by a SE, they were grown on SLG substrates for 45, 60, 75, and 90 min. In order to define the thickness of grown film, an appropriate optical model was constructed, and then the

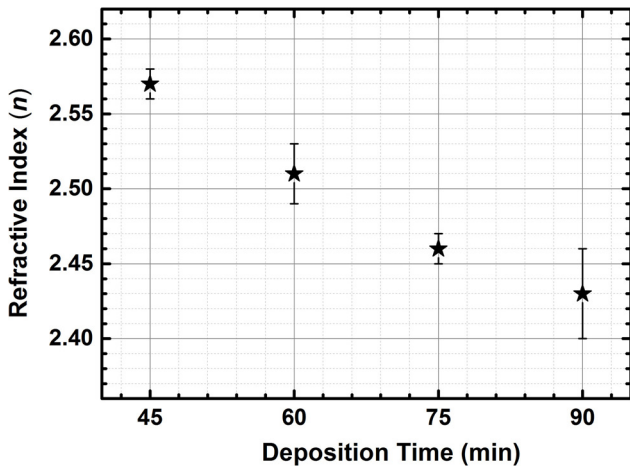


Figure 7. Refractive index variation with respect to deposition time of CdS films at 600 nm wavelength.

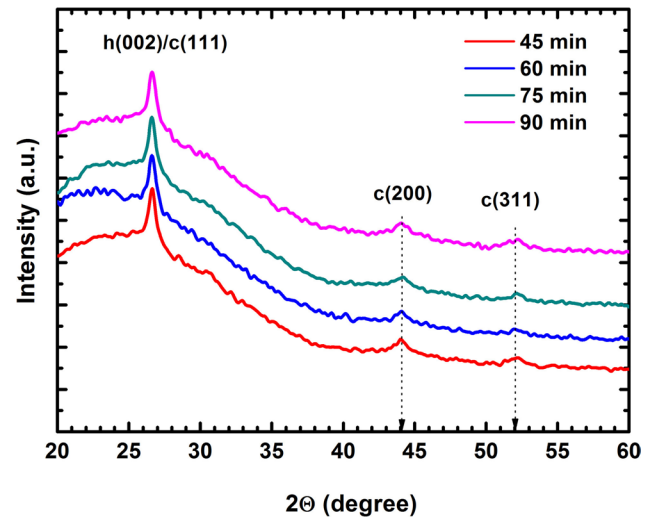


Figure 9. XRD spectra of CdS films grown at different deposition times.

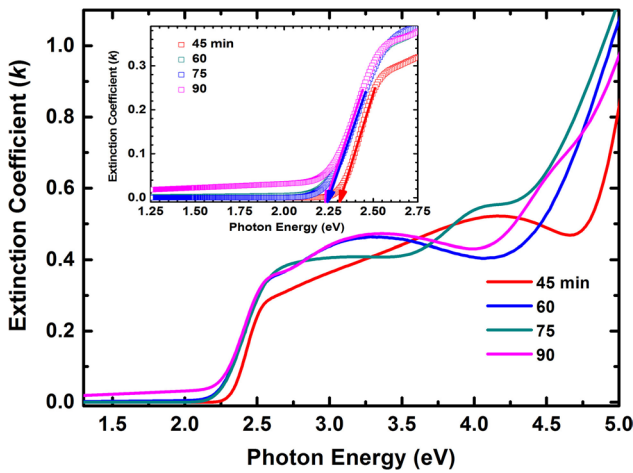


Figure 8. Distribution of extinction coefficient of CdS films with different thickness. The inset figure gives the bandgap determination of CdS films.

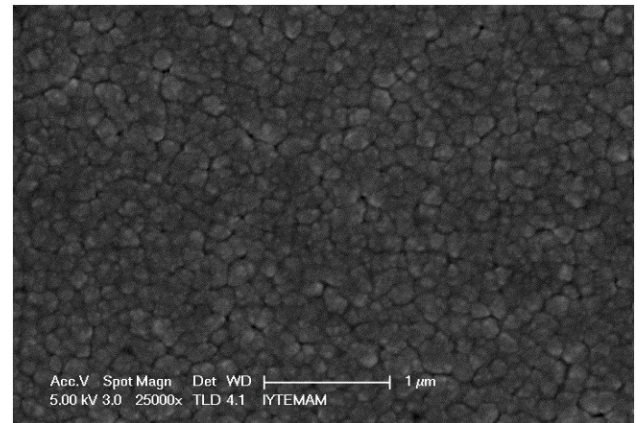


Figure 10. SEM image of thin CdS film grown on a SLG substrate for 75 min by the CBD technique.

measured and modeled ellipsometric data Psi ( $\Psi$ ) and Delta ( $\Delta$ ) were fitted, as given in figure 6.

Figures 6(a) and (b) show the fitting results of  $\Psi$  and  $\Delta$  of ellipsometric parameters for CdS films. In figure 6, small deviations can be observed between the experimental data and the model. This is because of the effect of depolarization, which is caused by the roughness and grain boundaries. At the end of the fitting of ellipsometric measurements with respect to the constructed model, the resulting CdS layer thicknesses were in the order of 85.0, 120.0, 133.0 and 148.0 nm for 45, 60, 75 and 90 min, respectively. The fitting results of a SE measurement of CdS films are listed in table 4 below.

As expected, the thickness of grown films increased with deposition time but the growth rate was different for each 15 min period. At the first time of deposition because the source materials were sufficiently existent, the ion-by-ion deposition process played a more crucial role than the cluster-by-cluster deposition process. After a while, due to the amount of source materials reduced, the cluster-by-cluster process became more dominant than the ion-by-ion process and decreased the deposition rate.

Table 5. EDX analyses of CdS thin films prepared using different deposition times.

Sample	Atomic% Cd	Atomic% S	Cd/S ratio	Thickness (nm)
45 min	57.15	42.85	1.33	85.0
60 min	57.05	42.95	1.33	120.0
75 min	53.68	46.32	1.16	133.0
90 min	52.63	47.37	1.11	148.0

Figure 7 shows the refractive index variation with respect to deposition time. The bulk CdS has a refractive index 2.52 at 2.06 eV photon energy (600 nm wavelength) [51]. The refractive index of CdS films decreased with the increase in deposition time.

The extinction coefficient  $k$ , was simulated with respect to photon energy at the end of the fitting procedure. The extinction coefficient of a material depends on its absorption. The optical bandgap ( $E_g$ ) of CdS films was determined from extrapolating the straight portion of the  $k$  versus the  $h\nu$  graph, on the  $h\nu$  axis at an absolute minimum of  $k$ . Figure 8 shows the distribution of the extinction coefficient with respect to

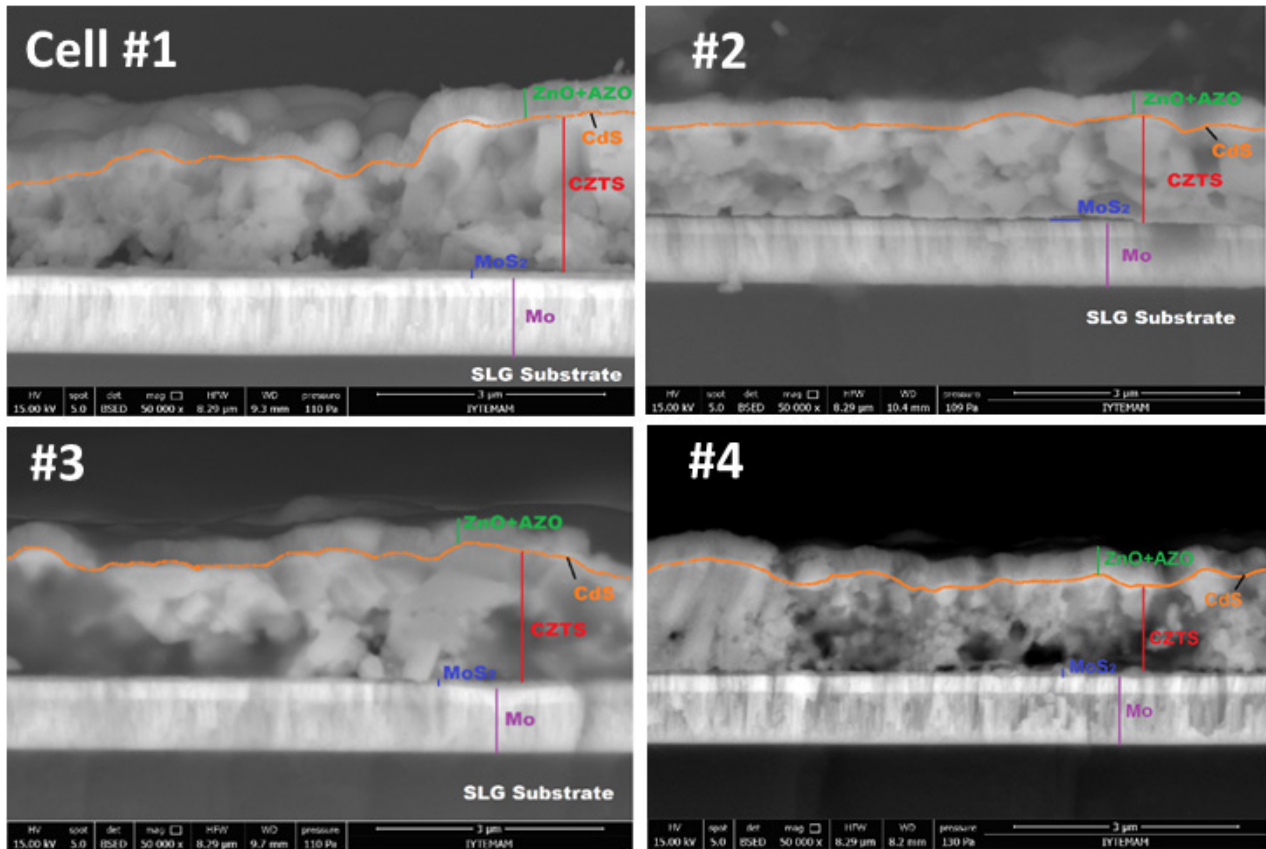


Figure 11. The SEM cross section of CZTS solar cells from 1 to 4.

photon energy and the inset figure demonstrates the bandgap determination. The optical bandgap of the CdS films reduced from 2.32 to 2.22 eV (from 45 min to 90 min deposition time). The reduction in the bandgap energy of the CdS buffer layer causes more absorption of incident light in this layer; as a result, the solar cell performance is adversely affected.

**3.2.2. XRD.** The crystallinity of CdS thin films having different thicknesses was confirmed by XRD. The crystal structure of CdS film can be pure hexagonal or in the cubic phase or a mixture of both [52]. In figure 9, all CdS films deposited for different time durations exhibited a similar XRD pattern.

Since the most intense diffraction angle position of hexagonal and cubic structures matches within 1%, determination of the exact crystal structure by XRD became difficult. The peak observed at 26.7° is given a (002) phase of hexagonal structure [53] whereas at 26.6° it represents the cubic structure of the (1 1 1) plane [54]. The second diffraction peak was detected at approximately 44.10° for all films; this corresponds to a (2 2 0) reflection of the cubic phase [55]. The third peak was encountered from 52.09 to 52.20° which is assigned to the (3 1 1) plane of the cubic CdS [55, 56].

**3.2.3. Surface morphology and composition.** The surface morphologies of the grown CdS thin films were monitored by SEM image analysis. As an illustration, the surface image of CdS film deposited for 75 min is shown in figure 10. CdS thin film has many small grains, which cover the substrate surface.

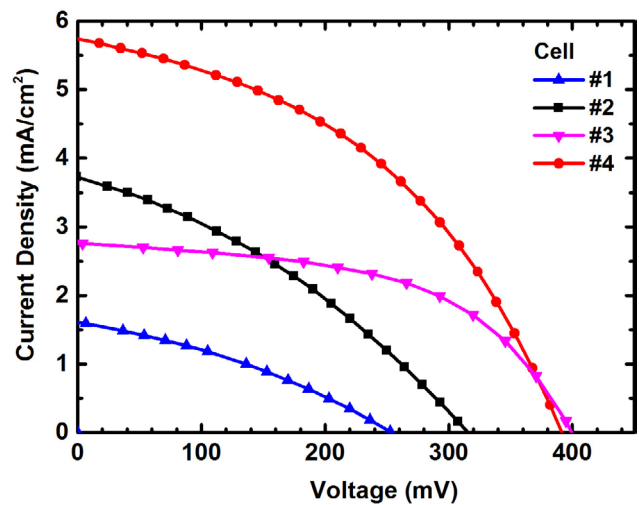


Figure 12. *J*-*V* curve of CZTS solar cells under illuminated conditions.

The atomic concentrations of the grown CdS films were determined by EDX analyses. Table 5 summarizes the atomic concentration and ratio of the Cd and S elements. EDS results showed that the all thin CDS films contain a higher amount of Cd than S. EDS results showed that a reduction in the Cd/S ratio in the solution was observed when the deposition time was higher than 60 min. This might be explained by the sedimentation of agglomerated clusters. Since the S vacancy ( $V_S$ ) acts as a shallow donor-type crystal defect, excess  $V_S$  increases

**Table 6.** Diode parameters of CZTS solar cell devices extracted from  $J$ - $V$  curves.

Cell	CdS thickness (nm)	$V_{OC}$ (mV)	$J_{SC}$ (mA cm <sup>-2</sup> )	FF (%)	$\eta$ (%)	$R_{SH}$ ( $\Omega$ cm <sup>2</sup> )	$R_S$ ( $\Omega$ cm <sup>2</sup> )
#1	140.0	255.3	1.62	32.9	0.14	282.2	97.3
#2	134.9	317.0	3.73	33.8	0.40	157.2	55.7
#3	102.5	402.0	2.76	53.8	0.60	692.0	37.3
#4	75.5	390.0	5.77	42.9	0.96	244.4	25.9

the n-type nature of CdS [57]. Therefore, a low deposition time is desired in terms of solar cell application.

### 3.3. Device characterizations

Next, we fabricated CZTS thin film solar cell devices with a substrate configuration of SLG/Mo/CZTS/CdS/ZnO/AZO. The cross-sectional SEM images of these devices are given in figure 11. These images show that some of the CZTS layers, used for device fabrications, include void formations. In the CZTS literature, it is often reported that the voids at the Mo-CZTS interface, which are called Kirkendall voids, form due to the different interdiffusion velocities of Cu, Zn, and Sn elements [58, 59]. From the SEM cross sections of devices shown in figure 11, the thicknesses of CdS buffer layers deposited for 90, 75, 60 and 45 min were measured as 140.0, 134.9, 102.5, and 75.5 nm for cells 1 to 4, respectively. SEM and SE results showed some variations in CdS buffer layers' thicknesses. The thicknesses of CdS buffer layers in device structures were slightly less than the values measured by a SE. The reason for this is that the CZTS absorber layer and the SLG substrate have different surface structures. Since the surface of SLG is much smoother than that of CZTS, the detected thicknesses were slightly different. From the SEM images shown in figure 11, the thicknesses of MoS<sub>2</sub> interface layers were measured as 118.80, 70.35, 86.50 and 48.86 nm for cells 1 to 4, respectively. This layer occurs due to the sulfurization of Mo back contact during the CZTS growth. Figure 12 gives some measured  $J$ - $V$  curves of corresponding CZTS solar cells under light illumination. The parameters obtained from such measurements are listed in table 6. As seen in figure 12 and table 6, solar cell number 4 with the thinnest CdS (75.5 nm) layer exhibited the highest  $J_{SC}$  and  $\eta$  values among all the devices with CdS buffer layers of 140.0, 134.9, 102.5, and 75.5 nm thicknesses for cells 1 to 4, respectively.

A straightforward method was used for estimating the series ( $R_S$ ) and the shunt resistance ( $R_{SH}$ ) of a solar cell. Table 6 demonstrates that the  $R_S$  highly depends on CdS thickness and decreases with the increasing thickness of a CdS buffer layer. The variations in the electrical characteristics with the buffer layer's thicknesses in all cells are listed in table 6. The  $V_{OC}$  increases with the decrease in the CdS thickness. However, a slight reduction in the  $V_{OC}$  was detected for cell 4, having the thinnest CdS buffer layer. This might be due to a reduction in the shunt resistance ( $R_{SH}$ ), which results from local imperfections in the bulk of CZTS or at the cell surface [60]. As seen in table 6, the  $V_{OC}$  and FF have similar variations with CdS thickness and  $J_{SC}$  was boosted from 1.62 to 5.77 mA cm<sup>-2</sup> with the thinner CdS layer due to the reductions in the absorption loss for short

wavelength light inside the buffer layer. Finally, by decreasing CdS thickness it was calculated that the efficiency value of the cell jumped from 0.14 to 0.96%. However, further reduction in the thickness of CdS resulted in a poorer PV response for the CZTS cell. This might result from an increase in the leakage current caused by pinhole formation in the CdS structure.

## 4. Conclusion

In this research, CZTS absorber layers were grown on Mo-coated SLG substrates using a two-stage process. Firstly, Cu-Zn-Sn metallic layers were sequentially deposited by a DC magnetron-sputtering technique and secondly, they were annealed under an Ar + S<sub>2</sub>(g) atmosphere. All CZTS absorber layers were prepared in Cu-poor and Zn-rich composition which is the desired composition for highly efficient CZTS-based solar cells. XRD measurements of the CZTS films revealed nearly the same diffraction spectra for all CZTS films whereby a kesterite formation in all absorber CZTS films was clearly observed. The kesterite and PD- kesterite CZTS structures were further confirmed by Raman analyses of the films. CdS, grown using the CBD technique, was used as a buffer layer. Optical characterization of CdS films on SLG demonstrated that the bandgap energy decreased with increment in the film's thickness. This result also caused enhancement of absorption in the CdS buffer layer. The SLG/Mo/CZTS/CdS/ZnO/AZO device structure was fabricated using a CdS buffer layer with four different thicknesses. The effect of the CdS buffer layer thickness on the PV response of CZTS solar cells was investigated from their  $J$ - $V$  curves.

According to our electrical measurement results,  $J_{SC}$  and  $\eta$  parameters were remarkably increased with the decreasing CdS thicknesses which might be explained by the reduction in the photon absorption losses in the thinner buffer layers. Significant improvements in efficiency were obtained for the device with the thinnest CdS (~75 nm) buffer layer but any further reduction in the CdS layer thickness deteriorated the diode properties of the CZTS cell. Thus, the best solar cell we produced had a  $V_{OC}$  of 390 mV, a  $J_{SC}$  of 5.77 mA cm<sup>-2</sup>, and an efficiency of 0.96%.

## Acknowledgments

This research was supported by The Scientific and Technological Research Council of Turkey (TUBITAK) with the project number of 114F341 and the Applied Quantum Research Center (AQuRec). We thank PhD candidate Merve Karakaya for spectroscopic ellipsometer measurements. We also thank to GUNAM for electrical measurements.

## ORCID iDs

A Cantas  <https://orcid.org/0000-0002-6536-5516>G Aygun  <https://orcid.org/0000-0003-0860-2914>

## References

- [1] Kumar M, Dubey A, Adhikari N, Venkatesan S and Qiao Q 2015 Strategic review of secondary phases, defects and defect-complexes in kesterite CZTSSe solar cells *Energ. Environ. Sci.* **8** 3134–59
- [2] Yoshikawa K, Kawasaki H, Yoshida W, Irie T, Konishi K, Nakano K, Uto T, Adachi D, Kanematsu M and Uzu H 2017 Silicon heterojunction solar cell with interdigitated back contacts for a photoconversion efficiency over 26% *Nat. Energy* **2** 17032
- [3] Jackson P, Wuerz R, Hariskos D, Lotter E, Witte W and Powalla M 2016 Effects of heavy alkali elements in Cu(In, Ga)Se<sub>2</sub> solar cells with efficiencies up to 22.6% *Phys. Status Solidi* **10** 583–6
- [4] Green M A, Hishikawa Y, Warta W, Dunlop E D, Levi D H, Hohl-Ebinger J and Ho-Baillie A W 2017 Solar cell efficiency tables (version 50) *Prog. Photovolt., Res. Appl.* **25** 668–76
- [5] Liyanage W P R and Nath M 2016 CdS–CdTe heterojunction nanotube arrays for efficient solar energy conversion *J. Mater. Chem. A* **4** 14637–48
- [6] Liu R, Tan M, Xu L, Zhang X, Chen J and Tang X 2016 Preparation of high-quality Cu<sub>2</sub>ZnSnS<sub>4</sub> thin films for solar cells via the improvement of sulfur partial pressure using a static annealing sulfurization approach *Sol. Energy Mater. Sol. Cells* **157** 221–8
- [7] Kim J, Hiroi H, Todorov T K, Gunawan O, Kuwahara M, Gokmen T, Nair D, Hopstaken M, Shin B and Lee Y S 2014 High efficiency Cu<sub>2</sub>ZnSn(S, Se)<sub>4</sub> solar cells by applying a double In<sub>2</sub>S<sub>3</sub>/CdS emitter *Adv. Mat.* **26** 7427–31
- [8] Lee Y S, Gershon T, Gunawan O, Todorov T K, Gokmen T, Virgus Y and Guha S 2015 Cu<sub>2</sub>ZnSnSe<sub>4</sub> thin-film solar cells by thermal co-evaporation with 11.6% efficiency and improved minority carrier diffusion length *Adv. Energy Mater.* **5** 1401372
- [9] Tajima S, Umehara M, Hasegawa M, Mise T and Itoh T 2017 Cu<sub>2</sub>ZnSnS<sub>4</sub> photovoltaic cell with improved efficiency fabricated by high-temperature annealing after CdS buffer-layer deposition *Prog. Photovolt., Res. Appl.* **25** 14–22
- [10] Shockley W and Queisser H J 1961 Detailed balance limit of efficiency of p-n junction solar cells *J. Appl. Phys.* **32** 510–9
- [11] Nagoya A, Asahi R, Wahl R and Kresse G 2010 Defect formation and phase stability of Cu<sub>2</sub>ZnSnS<sub>4</sub> photovoltaic material *Phys. Rev. B* **81** 113202
- [12] Buldu D G, Cantas A, Turkoglu F, Akca F G, Meric E, Ozdemir M, Tarhan E, Ozyuzer L and Aygun G 2018 Influence of sulfurization temperature on Cu<sub>2</sub>ZnSnS<sub>4</sub> absorber layer on flexible titanium substrates for thin film solar cells *Phys. Scr.* **93** 024002
- [13] Redinger A, Berg D M, Dale P J and Siebentritt S 2011 The consequences of kesterite equilibria for efficient solar cells *J. Am. Chem. Soc.* **133** 3320–3
- [14] Olgar M, Klaer J, Mainz R, Levenco S, Just J, Bacaksiz E and Unold T 2016 Effect of precursor stacking order and sulfurization temperature on compositional homogeneity of CZTS thin films *Thin Solid Films* **615** 402–8
- [15] Marchionna S, Garattini P, Le Donne A, Acciarri M, Tombolato S and Binetti S 2013 Cu<sub>2</sub>ZnSnS<sub>4</sub> solar cells grown by sulphurisation of sputtered metal precursors *Thin Solid Films* **542** 114–8
- [16] Wei Z, Newman M J, Tsoi W C and Watson T M 2016 Raman mapping analysis for removal of surface secondary phases of CZTS films using chemical etching *Appl. Phys. Lett.* **109** 123902
- [17] Meher S, Balakrishnan L and Alex Z 2016 Analysis of Cu<sub>2</sub>ZnSnS<sub>4</sub>/CdS based photovoltaic cell: a numerical simulation approach *Superlattices Microstruct.* **100** 703–22
- [18] Katagiri H, Saitoh K, Washio T, Shinohara H, Kurumadani T and Miyajima S 2001 Development of thin film solar cell based on Cu<sub>2</sub>ZnSnS<sub>4</sub> thin films *Sol. Energy Mater. Sol. Cells* **65** 141–8
- [19] Yazici S, Olgar M A, Akca F G, Cantas A, Kurt M, Aygun G, Tarhan E, Yanmaz E and Ozyuzer L 2015 Growth of Cu<sub>2</sub>ZnSnS<sub>4</sub> absorber layer on flexible metallic substrates for thin film solar cell applications *Thin Solid Films* **589** 563–73
- [20] Moriya K, Tanaka K and Uchiki H 2007 Fabrication of Cu<sub>2</sub>ZnSnS<sub>4</sub> thin-film solar cell prepared by pulsed laser deposition *Japan. J. Appl. Phys.* **46** 5780
- [21] Washio T, Shinji T, Tajima S, Fukano T, Motohiro T, Jimbo K and Katagiri H 2012 6% efficiency Cu<sub>2</sub>ZnSnS<sub>4</sub>-based thin film solar cells using oxide precursors by open atmosphere type CVD *J. Mater. Chem.* **22** 4021–4
- [22] Nakayama N and Ito K 1996 Sprayed films of stannite Cu<sub>2</sub>ZnSnS<sub>4</sub> *Appl. Surf. Sci.* **92** 171–5
- [23] Todorov T K, Reuter K B and Mitzi D B 2010 High-efficiency solar cell with earth-abundant liquid-processed absorber *Adv. Mater.* **22** E156–9
- [24] Scragg J J, Dale P J, Peter L M, Zoppi G and Forbes I 2008 New routes to sustainable photovoltaics: evaluation of Cu<sub>2</sub>ZnSnS<sub>4</sub> as an alternative absorber material *Phys. Status Solidi b* **245** 1772–8
- [25] Fujiwara H 2007 *Spectroscopic Ellipsometry: Principles and Applications* (New York: Wiley)
- [26] Cantas A, Aygun G and Basa D K 2014 *In situ* spectroscopic ellipsometry and structural study of HfO<sub>2</sub> thin films deposited by radio frequency magnetron sputtering *J. Appl. Phys.* **116** 083517
- [27] Olgar M, Klaer J, Mainz R, Ozyuzer L and Unold T 2017 Cu<sub>2</sub>ZnSnS<sub>4</sub>-based thin films and solar cells by rapid thermal annealing processing *Thin Solid Films* **628** 1–6
- [28] Cheng A-J, Manno M, Khare A, Leighton C, Campbell S and Aydil E 2011 Imaging and phase identification of Cu<sub>2</sub>ZnSnS<sub>4</sub> thin films using confocal Raman spectroscopy *J. Vac. Sci. Technol. A* **29** 051203
- [29] Lopez-Marino S et al 2016 The importance of back contact modification in Cu<sub>2</sub>ZnSnSe<sub>4</sub> solar cells: the role of a thin MoO<sub>2</sub> layer *Nano Energy* **26** 708–21
- [30] Abd-Elkader O H and Shaltout A A 2015 Characterization and antibacterial capabilities of nanocrystalline CdS thin films prepared by chemical bath deposition *Mater. Sci. Semicond. Process.* **35** 132–8
- [31] Yeh M-Y, Lei P-H, Lin S-H and Yang C-D 2016 Copper–zinc–tin–sulfur thin film using spin-coating technology *Materials* **9** 526
- [32] Skelton J M, Jackson A J, Dimitrievska M, Wallace S K and Walsh A 2015 Vibrational spectra and lattice thermal conductivity of kesterite-structured Cu<sub>2</sub>ZnSnS<sub>4</sub> and Cu<sub>2</sub>ZnSnSe<sub>4</sub> *APL Mater.* **3** 041102
- [33] Guç M, Levenco S, Bodnar I V, Izquierdo-Roca V, Fontane X, Volkova L V, Arushanov E and Pérez-Rodríguez A 2016 Polarized Raman scattering study of kesterite type Cu<sub>2</sub>ZnSnS<sub>4</sub> single crystals *Sci. Rep.* **6** 19414
- [34] Valakh M Y et al 2013 Raman scattering and disorder effect in Cu<sub>2</sub>ZnSnS<sub>4</sub> *Phys. Status Solidi Rap. Res. Lett.* **7** 258–61
- [35] Kaushik D K, Rao T N and Subrahmanyam A 2017 Studies on the disorder in DC magnetron sputtered Cu<sub>2</sub>ZnSnS<sub>4</sub> (CZTS) thin films grown in sulfide plasma *Surf. Coat. Technol.* **314** 85–91

- [36] Hall S R, Szymanski J T and Stewart J M 1978 Kesterite,  $\text{Cu}_2(\text{Zn,Fe})\text{SnS}_4$ , and stannite,  $\text{Cu}_2(\text{Fe,Zn})\text{SnS}_4$ , structurally similar but distinct minerals *Can. Mineral.* **16** 131–7
- [37] Schorr S, Hoebler H-J and Tovar M 2007 A neutron diffraction study of the stannite-kesterite solid solution series *Eur. J. Mineral.* **19** 65–73
- [38] Dumcenco D and Huang Y-S 2013 The vibrational properties study of kesterite  $\text{Cu}_2\text{ZnSnS}_4$  single crystals by using polarization dependent Raman spectroscopy *Opt. Mater.* **35** 419–25
- [39] Khare A, Himmetoglu B, Cococcioni M and Aydil E S 2012 First principles calculation of the electronic properties and lattice dynamics of  $\text{Cu}_2\text{ZnSn}(\text{S}_{1-x}\text{Se}_x)_4$  *J. Appl. Phys.* **111** 123704
- [40] Fernandes P, Salomé P and Da Cunha A 2011 Study of polycrystalline  $\text{Cu}_2\text{ZnSnS}_4$  films by Raman scattering *J. Alloys Compd.* **509** 7600–6
- [41] Dimitrievska M, Fairbrother A, Fontané X, Jawhari T, Izquierdo-Roca V, Saucedo E and Pérez-Rodríguez A 2014 Multiwavelength excitation Raman scattering study of polycrystalline kesterite  $\text{Cu}_2\text{ZnSnS}_4$  thin films *Appl. Phys. Lett.* **104** 021901
- [42] Mali S S, Patil B M, Betty C A, Bhosale P N, Oh Y W, Jadkar S R, Devan R S, Ma Y-R and Patil P S 2012 Novel synthesis of kesterite  $\text{Cu}_2\text{ZnSnS}_4$  nanoflakes by successive ionic layer adsorption and reaction technique: characterization and application *Electrochim. Acta* **66** 216–21
- [43] Ricardo C A, Su'ait M S, Müller M and Scardi P 2013 Production of  $\text{Cu}_2(\text{Zn, Fe})\text{SnS}_4$  powders for thin film solar cell by high energy ball milling *J. Power Sources* **230** 70–5
- [44] Yin X, Tang C, Chen M, Adams S, Wang H and Gong H 2013 Hierarchical porous  $\text{Cu}_2\text{ZnSnS}_4$  films for high-capacity reversible lithium storage applications *J. Mater. Chem. A* **1** 7927–32
- [45] Moholkar A, Shinde S, Babar A, Sim K-U, Kwon Y-B, Rajpure K, Patil P, Bhosale C and Kim J 2011 Development of CZTS thin films solar cells by pulsed laser deposition: influence of pulse repetition rate *Sol. Energy* **85** 1354–63
- [46] Ruan C-H, Huang C-C, Lin Y-J, He G-R, Chang H-C and Chen Y-H 2014 Electrical properties of  $\text{Cu}_x\text{Zn}_y\text{SnS}_4$  films with different Cu/Zn ratios *Thin Solid Films* **550** 525–9
- [47] Krylova V and Andrulevičius M 2009 Optical, XPS and XRD studies of semiconducting copper sulfide layers on a polyamide film *Int. J. Photoenergy* **2009** 304308
- [48] Deepu D R, Rajeshmon V G, Sudha Kartha C and Vijayakumar K P 2014 XPS depth profile study of sprayed CZTS thin films *AIP Conf. Proc.* **1591** 1666–8
- [49] Hurtado M, Cruz S D, Becerra R A, Calderón C, Bartolomé P and Gordillo G 2014 XPS analysis and structural characterization of CZTS thin films prepared using solution and vacuum based deposition techniques *IEEE 40th Photovoltaic Specialist Conf. (PVSC) (IEEE)* pp 368–72
- [50] Das S, Frye C, Muzykov P G and Mandal K C 2012 Deposition and characterization of low-cost spray pyrolyzed  $\text{Cu}_2\text{ZnSnS}_4$  (CZTS) thin-films for large-area high-efficiency heterojunction solar cells *ECS Trans.* **45** 153–61
- [51] Lisco F, Kaminski P M, Abbas A, Bowers J W, Claudio G, Losurdo M and Walls J 2015 High rate deposition of thin film cadmium sulphide by pulsed direct current magnetron sputtering *Thin Solid Films* **574** 43–51
- [52] Kumar M A and Muthukumaran S 2013 Effect of deposition time on structural, optical and photoluminescence properties of  $\text{Cd}_{0.9}\text{Zn}_{0.1}\text{S}$  thin films by chemical bath deposition method *J. Mater. Sci., Mater. Electron.* **24** 2858–65
- [53] Ezekoye B, Ighodalo K, Ezekoye V, Emeakaroha T, Ezema J and Offor P 2015 Nanocrystalline Cadmium sulfide (CdS) thin film synthesized at different dip times by chemical bath deposition technique *Int. J. Phys. Sci.* **10** 403–12
- [54] Kariper A, Guneri E, Gode F, Gumuş C and Ozpozan T 2011 The structural, electrical and optical properties of CdS thin films as a function of pH *Mater. Chem. Phys.* **129** 183–8
- [55] Fernando D, Khan M and Vasquez Y 2015 Control of the crystalline phase and morphology of CdS deposited on microstructured surfaces by chemical bath deposition *Mater. Sci. Semicond. Process.* **30** 174–80
- [56] Manikandan K, Dilip C S, Mani P and Prince J J 2015 Deposition and characterization of CdS nano thin film with complexing agent triethanolamine *Am. J. Eng. Appl. Sci.* **8** 318
- [57] Dávila-Pintle A, Lozada-Morales R, Palomino-Merino M R, Rivera-Márquez J A, Portillo-Moreno O and Zelaya-Ange O 2007 Electrical properties of Er-doped CdS thin films *J. Appl. Phys.* **101** 013712
- [58] Khalkar A, Lim K-S, Yu S-M, Shin D-W, Oh T-S and Yoo J-B 2015 Effects of sulfurization pressure on the conversion efficiency of cosputtered  $\text{Cu}_2\text{ZnSnS}_4$  thin film solar cells *Int. J. Photoenergy* **2015** 1–7
- [59] Tajima S, Itoh T, Hazama H, Ohishi K and Asahi R 2015 Improvement of the open-circuit voltage of  $\text{Cu}_2\text{ZnSnS}_4$  solar cells using a two-layer structure *Appl. Phys. Express* **8** 082302
- [60] Singh P and Ravindra N M 2012 Analysis of series and shunt resistance in silicon solar cells using single and double exponential models *Emerg. Mater. Res.* **1** 33–8